https://doi.org/10.5194/egusphere-2026-2689
Preprint. Discussion started: 9 July 2026

Prediction of precipitation-induced landslides and sediment discharge at the basin scale using machine learning

Riho Kido[1], Takuya Inoue[1,2], Kazuki Yamanoi[3]

[1] Graduate School of Advanced Science and Engineering, Hiroshima University, Hiroshima, 739-8527, Japan.
[2]Graduate School of Science and Technology, Gunma University, Gunma, 376-8515, Japan
[3]Disaster Prevention Research Institute, Kyoto University, Kyoto, 611-0011, Japan

Correspondence to: Takuya Inoue (inouetakuya@gunma-u.ac.jp)

Abstract. During heavy rainfall, sediment discharge from mountainous regions is exacerbating damage in downstream urban areas. Therefore, predicting sediment discharge from mountainous area is of critical importance. A large proportion of discharged sediment is produced by slope failures and subsequently transported through channel networks. Although topographic and geotechnical conditions vary within a watershed, both the susceptibility to slope failure and the volume of sediment produced depend strongly on these conditions. In this study, we develop a machine learning model that predicts slope failure occurrence and landslide volume from topographic and geotechnical parameters. By coupling this model with a rainfall and sediment runoff, we propose an integrated framework that simulates the entire process from slope failure to sediment production and downstream transport at the watershed scale. The proposed model incorporates uncertainties associated with unaccounted variability through a probabilistic representation, enabling the evaluation of multiple plausible scenarios. The model was applied to the Pekerebetsu basin for the 2016 Hokkaido heavy rainfall event. Repeated simulations under identical topographic, geotechnical, and rainfall conditions produced slightly different spatial patterns and numbers of slope failures. However, all simulations reproduced sediment production and discharge close to observed values. These results demonstrate that the proposed framework can consistently capture watershed-scale sediment dynamics while accounting for inherent variability in slope failure processes.

1 Introduction

Extreme rainfall due to climate change has caused severe flood disasters. These damages are not only attributed to increased discharge due to higher rainfall amounts, but also to the reduction in river conveyance capacity associated with sediment deposition transported from upstream areas (Sofia and Nikolopoulos 2020). Furthermore, the transported sediment affects riverbed morphology and channel dynamics, which can trigger additional hazards such as bank erosion (Inoue et al. 2021). To accurately predict sediment discharge, it is essential to quantify sediment production on hillslopes across a watershed scale, where diverse topographic and geotechnical conditions exist.

In mountainous watersheds, heavy rainfall events induce large volumes of sediment production through landslides. During such events, river discharge also increases, facilitating the downstream transport of produced sediment toward urban areas.

https://doi.org/10.5194/egusphere-2026-2689
Preprint. Discussion started: 9 July 2026

Although sediment discharge generally increases with rainfall under climate change, the relationship is non-linear (Kido et al. 2023). Therefore, it is crucial to evaluate both the susceptibility of hillslopes to failure and the volume of sediment produced during landslides, and to physically model the processes of sediment supply to channels and its downstream transport for watershed-scale sediment disaster risk assessment.

To evaluate rainfall-induced landslides, it is necessary to consider changes in soil moisture conditions due to rainfall infiltration and the resulting decrease in slope stability (Godt et al. 2008; Wicki et al. 2020; Posner and Georgakakos 2015). In infiltration analysis, water movement in unsaturated soil is simulated to obtain the spatiotemporal variation of pore-water pressure. In slope stability analysis, stability is evaluated using the factor of safety, defined as the ratio of resisting forces to driving forces. As rainfall infiltration increases pore-water pressure, the effective stress decreases due to buoyancy, reducing shear strength, while the increased water content adds weight, increasing driving forces (Iverson 2000). By using both infiltration and stability analysis, the failure process of slopes under rainfall can be mechanically evaluated. However, mountainous watersheds contain numerous slopes with heterogeneous topographic and geotechnical conditions, and the slopes that fail vary depending on rainfall patterns (Tsai 2008; Biasutti et al. 2016). Therefore, applying infiltration–stability analysis to all slopes within a watershed to evaluate failure occurrence and landslide volume is computationally expensive and impractical.

To address this issue, machine learning approaches have recently been proposed. For example, Bui et al. (2019) and Moayedi et al. (2019) showed that multilayer perceptrons and random forests perform well in predicting the factor of safety and slope failure using finite element simulation data. Xu et al. (2022) developed machine learning models as surrogates for computationally demanding physical models, and Mahmoodzadeh et al. (2022) constructed machine learning models for predicting the factor of safety under various geotechnical conditions. However, many of these studies assume temporally constant pore-water pressure and do not adequately consider its dynamic variation due to rainfall infiltration. One advantage of machine learning is its ability to account for uncertainty from large training datasets. Previous studies have used various input parameters, including slope gradient, slope length, cohesion, internal friction angle, density, hydraulic conductivity, and unit weight. Nevertheless, slope failure is influenced by additional factors, including topography, geology, vegetation, and hydrological conditions, which interact in a complex manner. Moreover, input parameters vary spatially within a slope, and a single value cannot adequately represent actual slope conditions. Therefore, explicitly representing such heterogeneity in numerical simulations remains challenging. Instead, it is more practical to perform probabilistic predictions under simplified homogeneous conditions and express the results as a range of possible failure responses, thereby implicitly accounting for the effects of unresolved heterogeneity. In addition, many existing studies focus on failure occurrence, while relatively few have examined the estimation of sediment volume produced by landslides.

In this study, we develop a machine learning model that predicts both slope failure occurrence and landslide volume from topographic and geotechnical parameters across diverse slope conditions. A probabilistic approach is adopted for failure prediction, allowing variability in outcomes even under identical conditions. Furthermore, by integrating this model with the rainfall and sediment runoff model that simulates temporal changes in soil moisture within slopes and the transport of produced

https://doi.org/10.5194/egusphere-2026-2689
Preprint. Discussion started: 9 July 2026

sediment, we aim to evaluate rainfall-induced sediment production and transport processes at the watershed scale and to reproduce past disaster events.

2 Method

2.1 Model of rainwater infiltration and Slope stability analysis

To evaluate failure occurrence and landslide volume for diverse slope conditions, we conducted rainfall infiltration and slope stability analyses using the model proposed by Tsutsumi (2008). The infiltration process of rainfall within the slope was simulated based on the Richards equation and C(ψ) and K(ψ) were evaluated using the log-normal model proposed by Kosugi (1996).

$$C(\psi)\frac{\partial \psi}{\partial t} = \nabla \cdot [K(\psi)\nabla(\psi + z)] \,, \tag{1}$$

$$C(\psi) = \frac{\theta_s - \theta_r}{\sqrt{2\pi}\sigma(-\psi)} exp\left\{-\frac{[\ln(\psi/\psi_m]^2}{2\sigma^2}\right\}, \tag{2}$$

$$K(\psi) = K_s\left[Q\left(\frac{\ln(\psi/\psi_m)}{\sigma}\right)\right]^{1/2}\left[Q\left(\frac{\ln(\psi/\psi_m}{\sigma}\sigma\right)\right]^2 , \tag{3}$$

$$Q(x) = \int_x^\infty \frac{1}{\sqrt{2\pi}} exp\left(-\frac{u^2}{2}\right) du \,, \tag{4}$$

Here, ψ denotes the pressure head, z is the elevation head, $C(\psi)$ is the soil water capacity, and $K(\psi)$ is the hydraulic conductivity. θ_s and θ_r represent the saturated and residual soil water contents, respectively. ψ_m is the pressure potential corresponding to the median soil pore radius, σ is a dimensionless parameter representing the pore-size distribution width, and K_s is the saturated hydraulic conductivity. The function $Q(x)$ denotes the residual normal distribution. Under saturated conditions ($\psi \geq$), $K(\psi) = K_s$ and $C(\psi) = 0.0$ were assumed.

The Richards equation was solved using the finite element method. The initial pressure head was uniformly set to −0.05 m throughout the soil layer. Based on Chen (2008), the parameters were set as $\theta_s = 0.467\ [m^3/m^3]$, $\theta_r = 0.240\ [m^3/m^3]$, $\psi_m = -31.2\ [cm]$, $\sigma = 1.4$, $K_s = 0.005\ cm/s$ uniformly to all slopes.

Slope stability analysis was performed using the simplified Janbu method, in which the soil layer is discretized into vertical slices and the ratio of driving to resisting forces is evaluated for each slice. The factor of safety (FoS) was calculated as:

$$F_s = \frac{\sum[\{c_i l_i \cos a_i + (W_i - u_i l_i \cos a_i)\tan\phi_i\}/m_a]}{\sum W_i \tan a_i}, \tag{5}$$

$$m_a = \cos^2 a_i\,(1 + \tan a_i \tan\phi_i / F_s) \,, \tag{6}$$

where subscript i denotes each vertical slice. c_i and ϕ_i are the cohesion and internal friction angle, respectively, W_i is the weight of the slice, a_i and l_i are the inclination angle and length of the slip surface, and $u_i$is the pore-water pressure acting on

https://doi.org/10.5194/egusphere-2026-2689
Preprint. Discussion started: 9 July 2026

the slip surface. The saturated unit weight used to compute W_i was set to $\gamma_{sat} = 1.64\ [t/m^3]$. The soil layer thickness was assumed to be uniform at 3 m.

The slip surface at each time step was determined as the one yielding the minimum factor of safety, which was identified using the dynamic programming (DP) method. The computational mesh size was set to 5 m in the horizontal direction and 0.33 m in the vertical direction.

2.2 Calculation condition of rainwater infiltration and Slope stability analysis

First, we conducted rainfall infiltration and slope stability analyses for various slopes with varying combinations of four parameters that can be relatively easily obtained from laboratory tests and DEM data: cohesion, internal friction angle, slope gradient, and slope length. The ranges of these parameters are summarized in Table 1. The “high-frequency region” represents parameter ranges that are considered common in natural environments, whereas the “low-frequency region” represents ranges that are relatively rare. By including samples from the low-frequency region, the prediction accuracy of the machine learning model for slopes with parameter values near the boundaries of the high-frequency region can be improved.

We generated a total of 1,200 slope configurations within the high-frequency region and 200 within the low-frequency region. To randomly generate combinations of slope parameters, Latin Hypercube Sampling (LHS) (McKay et al. 2000) was employed. In this method, each parameter range is uniformly divided into intervals, and one sample is drawn from each interval to ensure an efficient and well-distributed sampling of the parameter space. For slope length, LHS was applied in logarithmic space, because shorter slopes are expected to be more sensitive to changes in length in terms of landslide volume. This approach allows for denser sampling of shorter slopes.

The objective of the rainfall infiltration–based slope stability analysis is to determine the critical saturated layer height required for slope failure. The specific rainfall pattern is not explicitly considered, as the focus is on identifying the failure threshold. Instead, rainfall pattern is accounted for in the rainfall and sediment runoff model. Therefore, we designed the input rainfall to be sufficiently intense to induce failure in all slopes that are physically susceptible to collapse, while avoiding the Hortonian overland flow. Specifically, a hyetograph was applied in which rainfall intensity increases linearly from 0 to 50 mm/h over 12 hours, followed by a constant rainfall of 50 mm/h for 3 hours.

https://doi.org/10.5194/egusphere-2026-2689
Preprint. Discussion started: 9 July 2026

Table 1: Range of slope parameters used in the rainfall infiltration–based slope stability analysis.

	High-frequency region	Low-frequency region
Cohesion [tf/m^2]	0 - 1.5	1.5 - 3.0
Friction angle [degree]	20 - 40	10 -20, 40 - 45
Slope [degree]	20 - 45	10 – 20, 45 - 50
Length [m]	10 - 400	400 - 1000

2.3 Determination of slope failure by machine learning

Slope failure was determined based on a threshold defined by the critical saturation ratio at failure. The critical saturation ratio, θ_{cr}, was calculated as:

$$\theta_{cr} = h_{cr}/D_s \ , \tag{7}$$

Where h_{cr} is the critical saturated layer thickness and D_s is the soil depth. The value of h_{cr} was defined as the thickness of the soil layer in which the horizontally averaged pressure head is greater than or equal to zero.

The critical saturated layer thickness h_{cr} was estimated by assuming a linear variation of pressure head between adjacent nodes. For two consecutive points where $\psi_1 > 0$ and $\psi_2 < 0$, h_{cr} was calculated by linear interpolation as:

$$h_{cr} = h_1 + \frac{0-\psi_1}{\psi_2-\psi_1}(h_2 - h_1) \ , \tag{8}$$

where h_1 and h_2 are the elevations corresponding to ψ_1 and ψ_2, respectively. If the pressure head at the top layer was greater than or equal to zero, the entire soil depth was considered saturated (i.e., $h_{cr} = D_s$).

We developed a machine learning model for slope failure prediction using four slope parameters (cohesion, internal friction angle, slope gradient, and slope length) as explanatory variables and the saturation degree at failure (or at the end of the simulation for stable slopes) derived from rainfall infiltration–based slope stability analysis as censored data.. For this purpose, we adopted the Random Survival Forest (RSF) model. This is an extension of the Random Forest (RF) model to survival analysis, which can account for censored data (i.e., cases where failure does not occur within the simulation period). Using RSF model, information from non-failed slopes can also be incorporated into the training process, enabling probabilistic slope failure assessment.

https://doi.org/10.5194/egusphere-2026-2689
Preprint. Discussion started: 9 July 2026

In survival analysis, the probability that an event does not occur up to a given time is estimated as the survival probability $S(t)$, obtained by multiplying conditional survival probabilities over time. In this study, "time" was replaced by the saturation ratio, enabling the estimation of the probability of failure occurrence at different saturation levels.

The hyperparameters were set as follows: 1,500 decision trees, a minimum of 2 samples required for node splitting, a minimum of 5 samples per leaf node, and no limit on the maximum tree depth. From the trained RSF model, the survival probability $S_j(\theta_i)$ at nine discrete saturation levels θ_i (from 0.1 to 0.9 with an interval of 0.1) was assigned to each slope element j with different geotechnical and topographic conditions. When the saturation ratio θ calculated by the rainfall and sediment runoff model first exceeded a given threshold θ_i, slope failure was probabilistically determined. Specifically, failure was assumed to occur when a uniformly distributed random number was smaller than the conditional failure probability $P_{failure}$ defined as:

$$P_{failure} = 1 - \frac{S_j(\theta_i)}{S_j(\theta_{i-1})} \quad (\theta_i = 0.1,\ 0.2,\ \ldots,\ 0.9) \quad , \tag{9}$$

2.4 Estimation of failure volume by machine learning

In the rainfall infiltration–slope stability analysis, we obtained landslide area A. A uniform soil depth of 3 m is assumed in this analysis. This assumption is supported by the strong empirical relationship between landslide volume V_L and landslide area A_L, commonly expressed as $V_L = \alpha A_L^{\beta}$ (Amirahmadi et al. 2016; Guzzetti et al. 2009; Rice and Foggin 1971; Imaizumi et al. 2008). Assuming a constant soil depth D_s, landslide volume can be approximated as $V_L = A_L D_s$, implying a linear relationship between volume and area. Although the coefficients α and β vary among regions, they can often be approximated as constant within a single watershed, suggesting that the effect of spatial variability in soil depth is effectively incorporated into these empirical parameters. Thus, although the assumption of a constant soil depth does not explicitly represent local variations in soil depth, it can be regarded as a practical first-order approximation for watershed-scale sediment production modelling. Therefore, we estimated the failure length, L by following equation, rather than the landslide area itself

$$L = A/D_s \ , \tag{10}$$

We adopted the Random Forest (RF) model to estimate the failure length from slope parameters. In this model, cohesion, internal friction angle, slope gradient, and slope length were used as explanatory variables, whereas the failure length was used as the target variable. The RF model constructs a large number of decision trees using subsets of the data and produces predictions by averaging their outputs. This approach is suitable because failure length is expected to depend nonlinearly on geotechnical and topographic parameters, such as cohesion, internal friction angle, slope gradient, and slope length, and on their interactions. Using the trained RF model, the failure length L_j was predicted for each slope element j.

The landslide volume V_j for each slope element j was calculated as:

$$V_j = L_j \times D_{s_j} \times B_j \ , \tag{11}$$

https://doi.org/10.5194/egusphere-2026-2689
Preprint. Discussion started: 9 July 2026

where D_{s_j} is the soil depth and B_j is the width of the slope element.

When slope failure occurs with the probability P_{failure}, the corresponding sediment volume V_j is produced.

175

2.5 Rainfall and sediment runoff model

To simulate sediment production by slope failures, sediment supply to channels, and sediment transport within the river network under rainfall input, we used the SiMHiS model developed by Yamanoi et al. (2015, 2016a, 2016b), with modifications to account for channel width variation (Kido et al. 2025).

180 SiMHiS discretizes a watershed into unit channels divided at confluences and unit slopes adjacent to both banks. Sediment produced by slope failures on unit slopes is supplied to the adjacent unit channels, where bedload and suspended load transport are simulated. Slope failure is evaluated at a finer scale using slope elements, which are defined by further subdividing unit slopes along ridge and valley lines to prevent lateral water movement between neighboring slopes (Xie et al. 2003).

Within each slope element, subsurface water flow is computed using a kinematic wave model. The subsurface discharge per

185 unit width, q_r is calculated based on Darcy's law, while when the water level exceeds the soil depth, overland flow is generated and computed using Manning's equation.

$$\frac{dq_r}{dx} + \alpha \frac{dh_r}{dt} = r - f \,, \tag{12}$$

$$q_r = \begin{cases} kh_r & (h_r \le D_s) \\ kD_s + \frac{1}{n_s}(h_r - D_s) & (h_r > D_s) \end{cases}, \tag{13}$$

$$q_{bk}^* = \alpha(\tau_{*k} - \tau_{*ck})^{1.5} \,, \tag{14}$$

190 Here, q_r is the unit-width discharge within the slope, h_r is the water depth within the soil layer, r is the rainfall intensity, f is the loss rate per unit time, λ is the porosity, k is the hydraulic conductivity, n_s is the Manning's roughness coefficient for the slope surface. In addition, q_{bk}^* denotes the dimensionless bedload transport rate per unit width for each grain size class, τ_{*k} is the dimensionless shear stress, and τ_{*ck} is the dimensionless critical shear stress for each grain size.

Next, in the sediment supply model, the amount of sediment supplied from slopes to channels is calculated. Sediment produced

195 by slope failures is assumed to accumulate temporarily as colluvial deposits, and only the portion exceeding the storage capacity is supplied to the channel.

Finally, in the sediment transport model, bedload and suspended load transport are calculated, considering erosion and deposition processes along the riverbed. Flow discharge is computed using a kinematic wave model to represent the process by which rainfall on slopes flows into the channel network, while channel flow is calculated using Manning's equation.

200 The bedload transport rate is estimated using a Meyer–Peter–Müller-type formulation (24), combined with the Johnson model (Johnson 2016) and a modified Egiazaroff equation (Egiazaroff 1965) to evaluate the dimensionless critical shear stress.

https://doi.org/10.5194/egusphere-2026-2689
Preprint. Discussion started: 9 July 2026

Although many bedload transport formulas adopt a power-law form proportional to $\tau_*^{1.5}$, as in the MPM equation, the coefficient α is empirically determined. For example, Jafar (2025) reported a value of 12.49 based on field data from rivers worldwide, Ashida Michiue(1972) proposed 17, and Shinohara (1959) suggested 25. In this study, α is set to 23 to reproduce observed sediment discharge.

The suspended load transport rate was calculated using the Itakura–Kishi formula (Itakura and Kishi 1980) together with Rubey's settling velocity equation (Rubey 1933).

2.6 Application in the Pekerebetsu basin with SiMHiS

The machine learning models developed using the methods described in Sect. 2.3 and 2.4 were integrated into the SiMHiS framework to reproduce sediment production and sediment discharge during the August 2016 heavy rainfall event in the upper reaches of the Pekerebetsu River, a tributary of the Tokachi River system in Hokkaido, Japan.

The mean annual precipitation in the Tokachi River basin from 1966 to 2005 was approximately 900 mm, which is significantly lower than the national average of about 1,600 mm in Japan (River Bureau, Ministry of Land, Infrastructure, Transport and Tourism 2006). In late August 2016, heavy rainfall caused by a stationary front and multiple typhoons triggered widespread flooding and landslides across the Tokachi River basin, resulting in severe damage. In this study area, orographic rainfall was intensified by the transport of warm, moist air associated with typhoons, and the cumulative rainfall exceeded 500 mm over three days (Aoki et al. 2018). Figure 1 shows the rainfall in the Pekerebetsu basin based on AMeDAS data provided by the Japan Weather Association. On August 30, the maximum hourly rainfall reached 50 mm/h. Miyazaki reported sediment production from slopes of 154,000 m³ and sediment discharge of 373,000 m³ during this event (Miyazaki et al. 2016).

The Pekerebetsu River basin is primarily composed of weathered granite. Laboratory test (Sato et al. 2016) results indicate that cohesion ranges from 0.07 to 0.53 tf/m² depending on the degree of compaction, while the internal friction angle varies from 35.6° to 38.9°. Since cohesion in natural slopes is influenced by root reinforcement and soil heterogeneity, a sensitivity analysis was conducted based on this range. In contrast, the variation in internal friction angle is relatively small. Therefore, the mean value of 37.3° was adopted. Miyazaki et al. 2016 investigated the grain size distribution of terraces and cliff cones in this area. We used the grain size distribution of the terrace to represent riverbed sediment, and that of the cliff cone to represent slope-derived sediment. The average grain size of the riverbed sediment is 162 mm, whereas that of slope sediment is 70 mm, indicating that the slope sediment was finer than the riverbed sediment.

Slope elements were delineated from a 10 m resolution DEM acquired by LiDAR prior to the 2016 flood event, and topographic parameters such as slope gradient and slope length were calculated for each slope element.

The slope parameters for each slope element were then input into the trained machine learning models to estimate the failure probability at different saturation levels and the corresponding landslide volume. By inputting the observed rainfall data of the 2016 event into the SiMHiS model, the temporal variation of saturation within slopes was computed, and slope failure

https://doi.org/10.5194/egusphere-2026-2689
Preprint. Discussion started: 9 July 2026

occurrence and sediment production across the watershed were estimated. Then we compared the simulated sediment production with observed values.

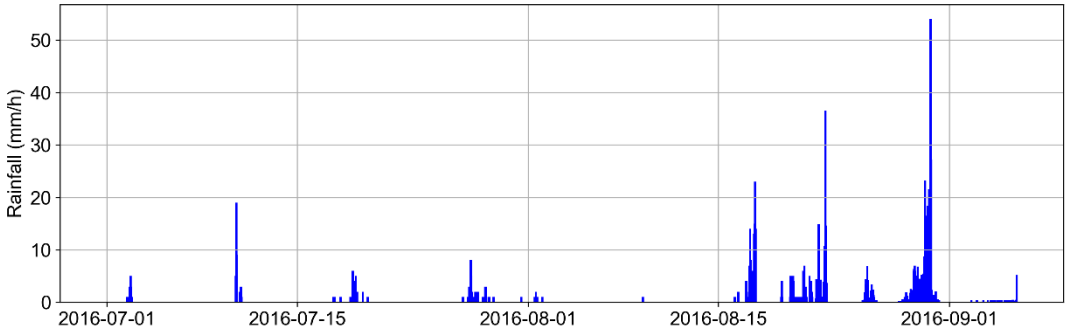

Figure 1: AMeDAS rainfall in the Pekerebetsu basin during the 2016 Hokkaido heavy rainfall event.

3 Result

3.1 Result of rainwater infiltration and Slope stability analysis

Figure 2(a) shows the classification results of slope stability for the four slope parameters, categorized into three groups: stable slopes where no failure occurred, slopes that failed during the simulation, and slopes that were unstable and failed immediately at the start of the calculation. Among the 1,400 simulation cases, 717 cases (51%) remained stable, 450 cases (32%) experienced failure during the simulation, and 233 cases (17%) failed immediately without maintaining initial stability. Cohesion, internal friction angle, and slope gradient interactively influence slope stability. Higher cohesion, larger internal friction angles, and gentler slopes tend to suppress failure. In contrast, slope length has little influence on stability.

Figure 2(b) shows the saturation ratio at the time of failure for slopes that collapsed during the simulation. Similar to the stability classification results, cohesion, internal friction angle, and slope gradient strongly influence the critical saturation ratio, whereas slope length has negligible impact.

Figure 2(c) presents the failure length for slopes that experienced rainfall-induced collapse during the simulation. For slopes longer than 15 m, the failure length tends to converge within the range of approximately 15–20 m. In addition, under particularly stable slope conditions, failure lengths exceeding 20 m were observed.

https://doi.org/10.5194/egusphere-2026-2689
Preprint. Discussion started: 9 July 2026

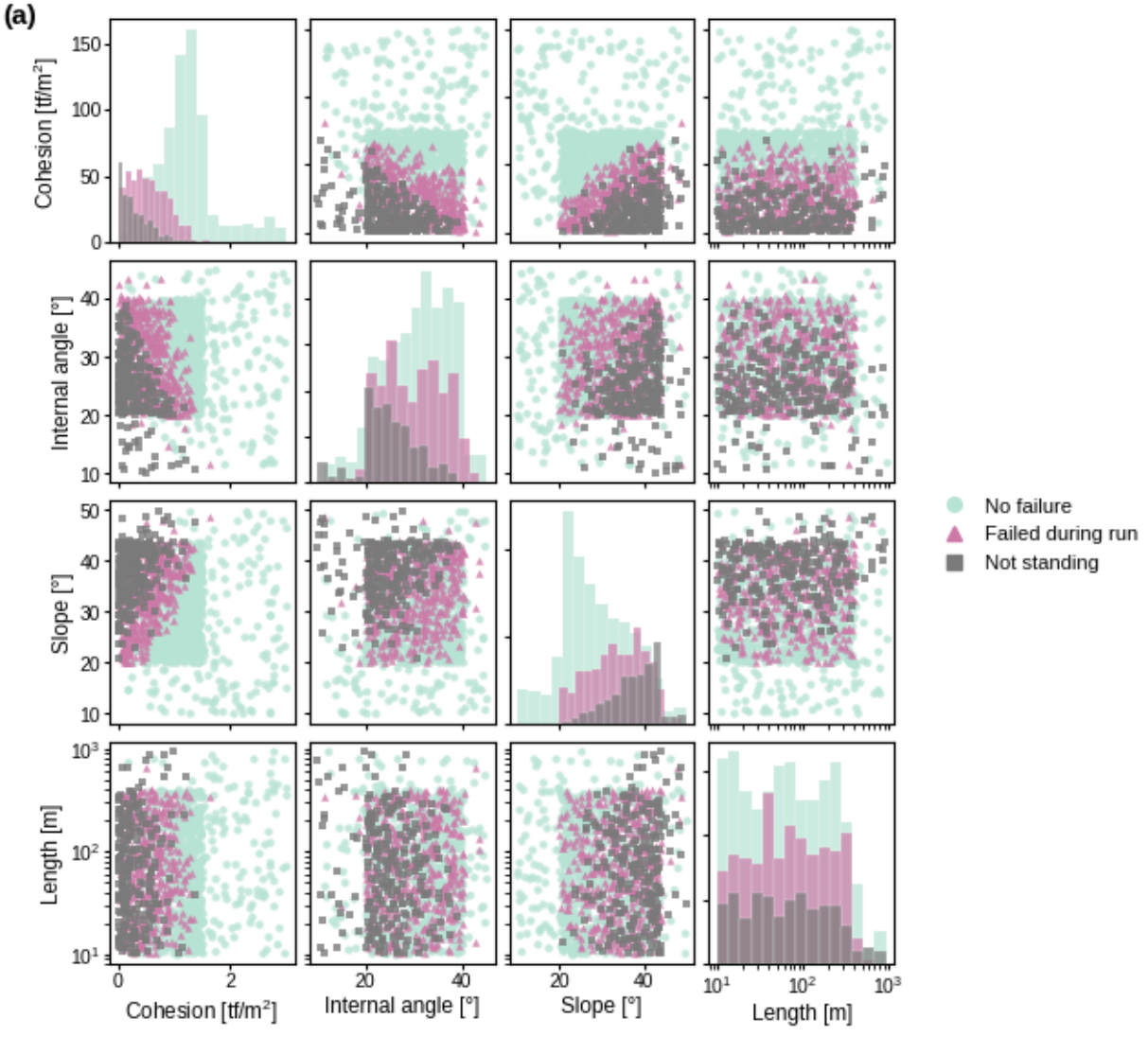

https://doi.org/10.5194/egusphere-2026-2689
Preprint. Discussion started: 9 July 2026

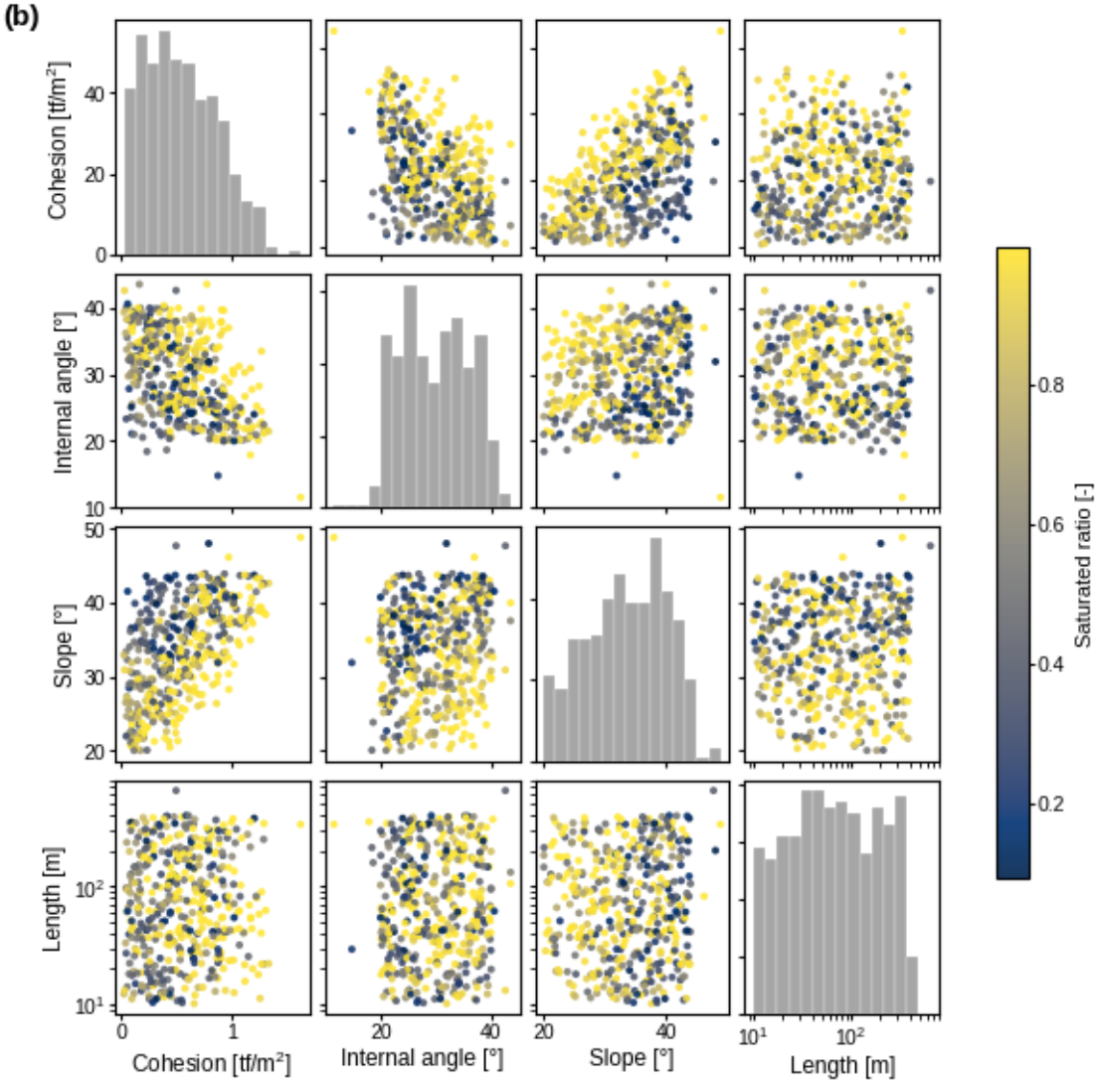

https://doi.org/10.5194/egusphere-2026-2689
Preprint. Discussion started: 9 July 2026

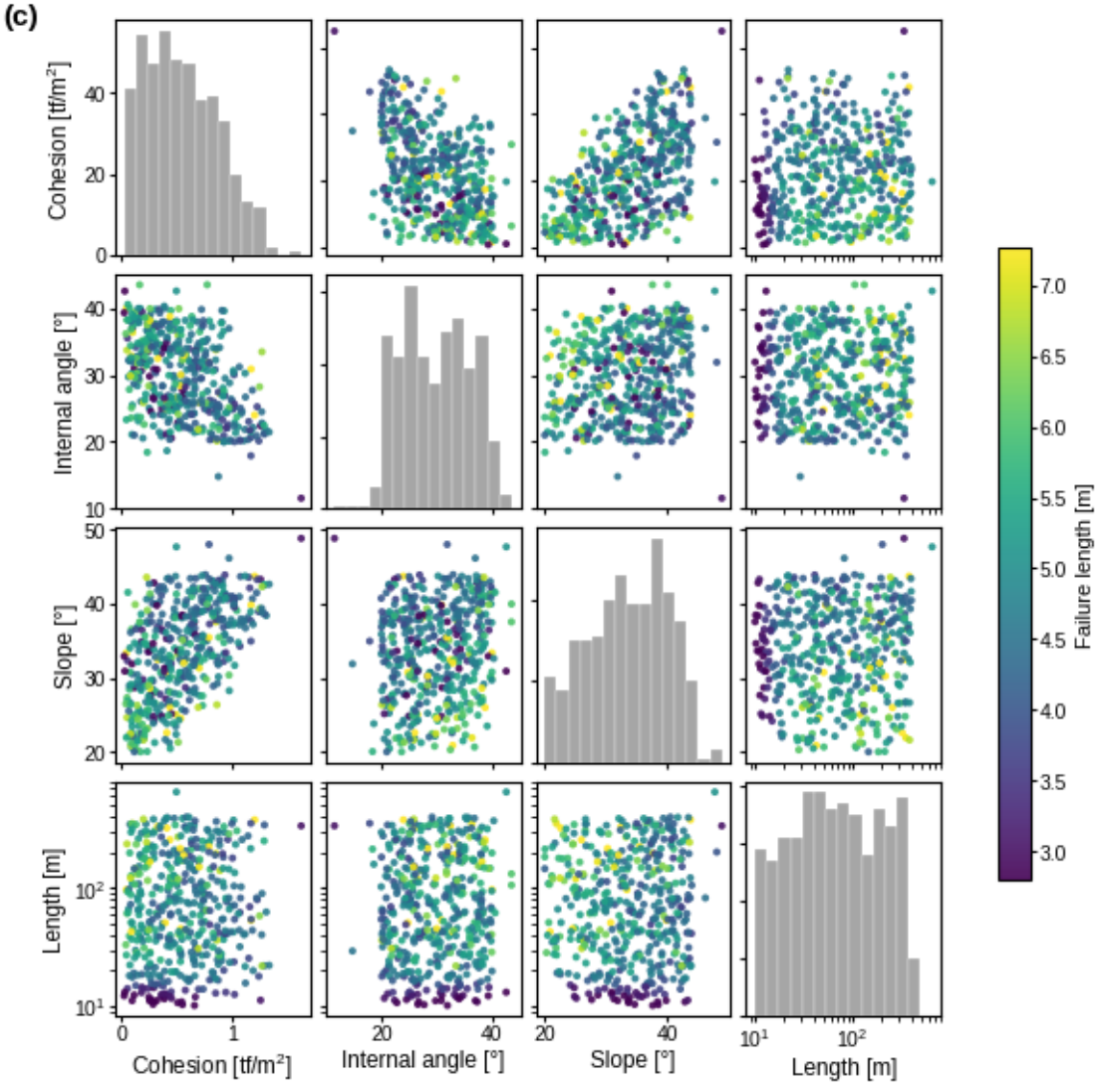

Figure 2: (a) Classification of slope stability results for the simulated slopes according to four slope parameters. Blue indicates stable slopes, orange indicates slopes that failed during the simulation, and green indicates slopes that failed immediately at the start of the simulation.

(b) Saturation degree at the time of failure for failed slopes as a function of the four slope parameters.

(c) Failure length of failed slopes as a function of the four slope parameters.

https://doi.org/10.5194/egusphere-2026-2689
Preprint. Discussion started: 9 July 2026

3.2 Result of slope failure determination

The area under the ROC curve in Figure 3(a) (AUC) for the test dataset is 0.89, suggesting that the model has sufficient discriminative capability for predicting slope failure.

Figure 3(b) shows the failure probability obtained from the rainfall infiltration–slope stability analysis and that predicted by the RSF model for the test dataset. In this study, we used a bootstrap approach to evaluate slope failure probability. Specifically, 180 slopes were randomly sampled with replacement from the test dataset to form one slope group, and this procedure was repeated 200 times. For each slope group, a failure probability curve was estimated based on the slope stability analysis results using the Kaplan–Meier method (Kaplan and Meier, 1958), resulting in a total of 200 failure probability curves. From these curves, the average and the 95% interval (5th–95th percentile range) were calculated.

For the RSF-based estimation, we used the same bootstrap-generated slope groups. For each slope group, failure probability curves were estimated for all 180 slopes, and these were averaged at each saturation level to obtain a representative curve. Repeating this process 200 times yielded 200 curves, from which the average and 95% interval were computed.

The failure probabilities predicted by the RSF model are generally consistent with those obtained from the slope stability analysis, indicating that the RSF model successfully reproduces the relationship between saturation and failure probability. However, the 95% interval derived from the slope stability analysis extends toward higher failure probabilities compared to that of the RSF predictions.

Figure 3(c) shows the relationship between saturation ratio and failure probability for different ranges of slope parameters. Each curve represents the average response of slopes belonging to the corresponding parameter range. Slopes with cohesion less than 0.5 tf/m² and internal friction angles less than 25° exhibit higher failure probabilities in the slope stability analysis than those predicted by the RSF model. This suggests that slope groups containing slopes highly susceptible to failure contribute to the upward shift of the 95th percentile in Figure 3(a). In addition, slopes with cohesion below 0.5 tf/m² show significantly higher failure probabilities than the average, whereas slopes with cohesion greater than 1.0 tf/m² exhibit very low failure probabilities, indicating that cohesion has a stronger influence on failure probability than the other parameters. Regarding slope gradient, failure probability appears to be bifurcated around the median internal friction angle (30°) of the high-frequency region. When the slope gradient exceeds the internal friction angle, instability increases, indicating that the relative relationship between these parameters controls slope stability.

Figure 3(d) compares the predicted and simulated failure lengths for both the training and test datasets. The RF model tends to underestimate failure length in cases with large failure areas. This is because large-failure cases are relatively rare and are grouped into the same terminal nodes as smaller cases during tree construction. However, since such large-scale failures occur infrequently, their impact on watershed-scale predictions is considered limited.

https://doi.org/10.5194/egusphere-2026-2689
Preprint. Discussion started: 9 July 2026

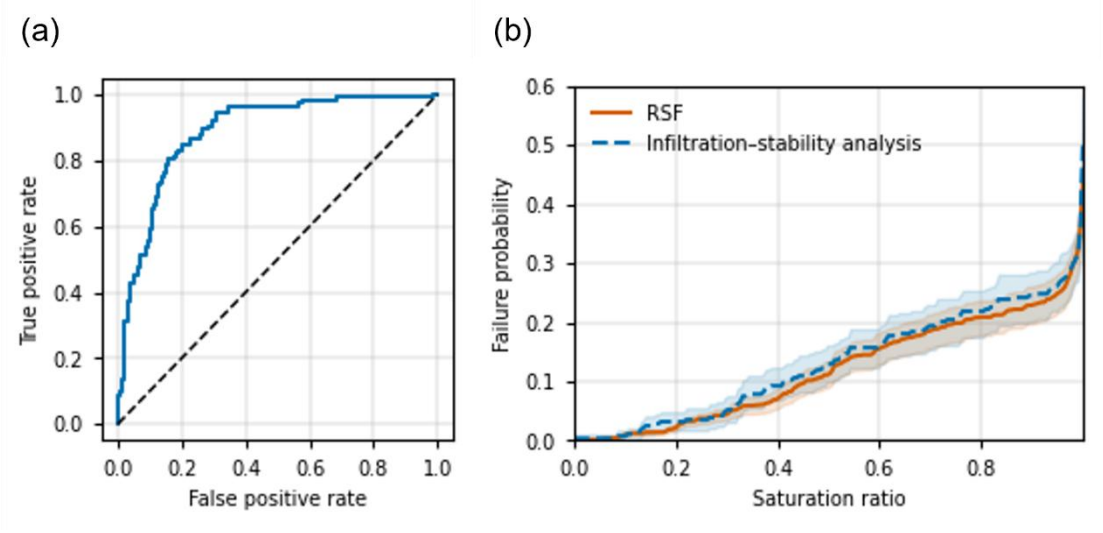

290

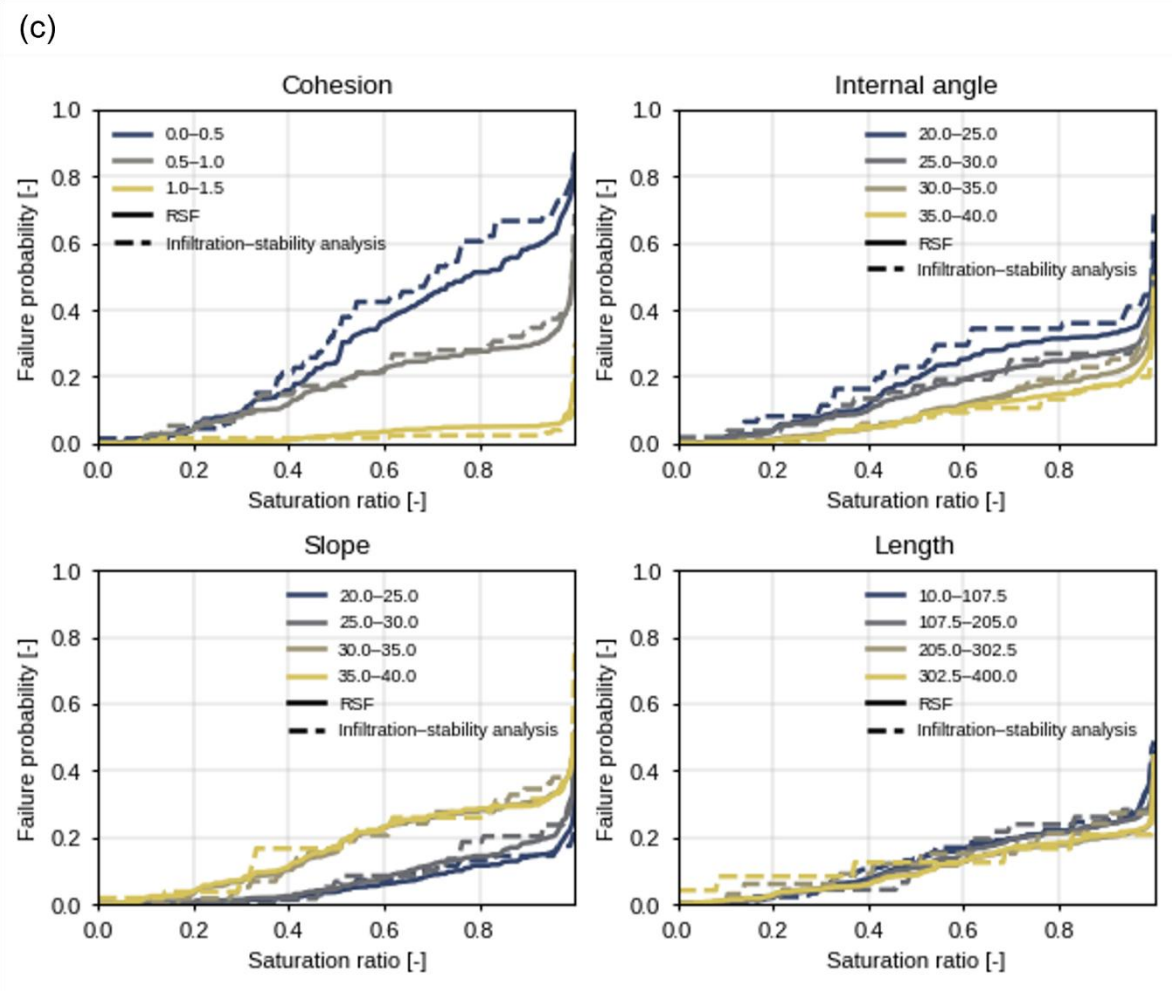

https://doi.org/10.5194/egusphere-2026-2689
Preprint. Discussion started: 9 July 2026

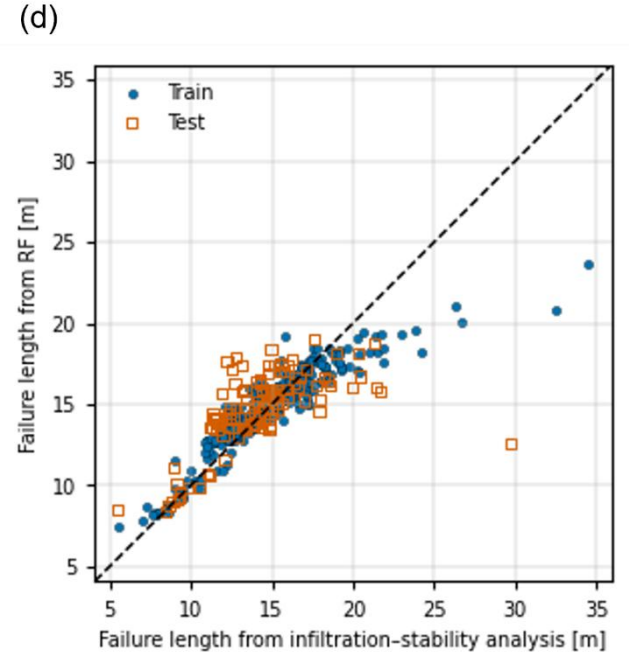

Figure 3: (a) ROC curve for the RSF-based slope failure prediction in the hold-out test dataset.
(b) Relationship between saturation degree and failure probability. Blue lines indicate failure probabilities obtained from rainfall infiltration–based slope stability analysis, while orange lines indicate those predicted by the RSF model. Shaded areas represent the 95% interval for each.
(c) Relationship between saturation degree and failure probability for different parameter ranges. Dashed lines indicate results from the slope stability analysis, whereas solid lines represent predictions by the RSF model.
(d) Comparison between failure lengths calculated by the rainfall infiltration–based slope stability analysis and those predicted by the RF model. Blue points indicate training data, and white points indicate validation data.

3.3 Result of slope failure determination

When cohesion is 0.95 tf/m², we performed three simulations under the same rainfall and model conditions as those of the 2016 heavy rainfall event in Hokkaido. Table 2 summarizes the number of failed slope elements, the failure ratio, the produced sediment volume, and the sediment discharge. The failure ratio was calculated as the number of failed slope elements divided by the total number of slope elements in the basin, 3,720. The produced sediment by slope failures is from 148,830 m³ to 161,937 m³ and a sediment discharge is from 372,880 m³ to 376,328 m³, successfully reproducing the sediment production and discharge observed during the 2016 heavy rainfall event in Hokkaido. Figure 4 shows the failure probability and failure length at a saturation ratio of 0.99 when cohesion ranges from 0.1 to 1.1 tf/m² at intervals of 0.1 tf/m² and the internal friction angle is fixed at 37.3°, based on the properties observed in the Pekerebetsu basin. White areas indicate combinations of slope

https://doi.org/10.5194/egusphere-2026-2689
Preprint. Discussion started: 9 July 2026

gradient and slope length that do not exist within this basin. The results show that failure probability increases with decreasing cohesion and increasing slope gradient. In contrast, failure length decreases as cohesion decreases and slope gradient increases. Furthermore, for slopes steeper than approximately 28°, shorter slopes tend to exhibit shorter failure lengths.

Figure 5 presents the produced sediment due to slope failures, sediment discharge by source (riverbank, slope, bank), and the average grain size of discharged sediment for each cohesion value. Both the produced sediment and the total sediment discharge decrease as cohesion increases. When cohesion is less than or equal to 0.7 tf/m², the amount of produced sediment by slope failures exceeds the sediment discharge, indicating that more than half of the discharged sediment originates from slopes. In contrast, when cohesion is greater than or equal to 0.9 tf/m², the produced sediment is smaller than the sediment discharge, suggesting that most of the discharged sediment is generated by erosion of the riverbed and banks. Additionally, as the contribution of produced sediment decreases, the average grain size of the discharged sediment increases. Figure 6 shows the spatial distribution of failed slopes for three simulations conducted under identical conditions corresponding to the 2016 event. As shown in Figure 6, areas with a high density of steep slopes tend to have a larger number of failed slope elements. However, the locations of failed slopes vary slightly among simulations. As indicated in Table 2, a greater number of failed slopes does not necessarily result in a larger volume of produced sediment. Even under identical conditions, differences in the spatial distribution of failed slopes lead to variations in the scale of sediment production. Furthermore, even produced sediment is large, sediment discharge does not always increase proportionally. This suggests that the connectivity between failed slopes and the channel network strongly controls the efficiency of sediment transport from production areas to the downstream.

https://doi.org/10.5194/egusphere-2026-2689
Preprint. Discussion started: 9 July 2026

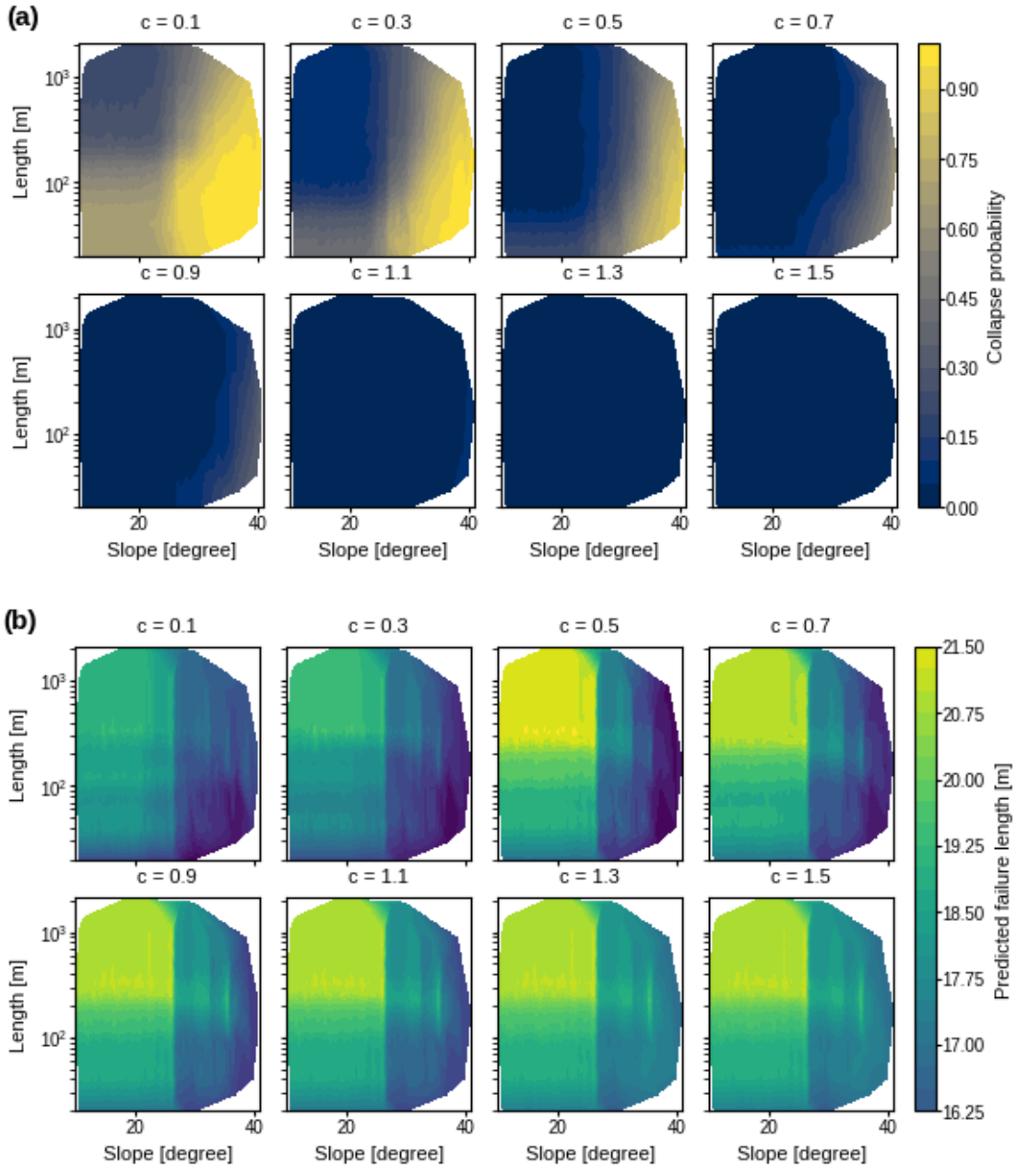

330 **Figure 4: Failure probability (a) and failure length (b) at a saturation ratio of 0.99 for different cohesion values in the Pekerebetsu basin.**

https://doi.org/10.5194/egusphere-2026-2689
Preprint. Discussion started: 9 July 2026

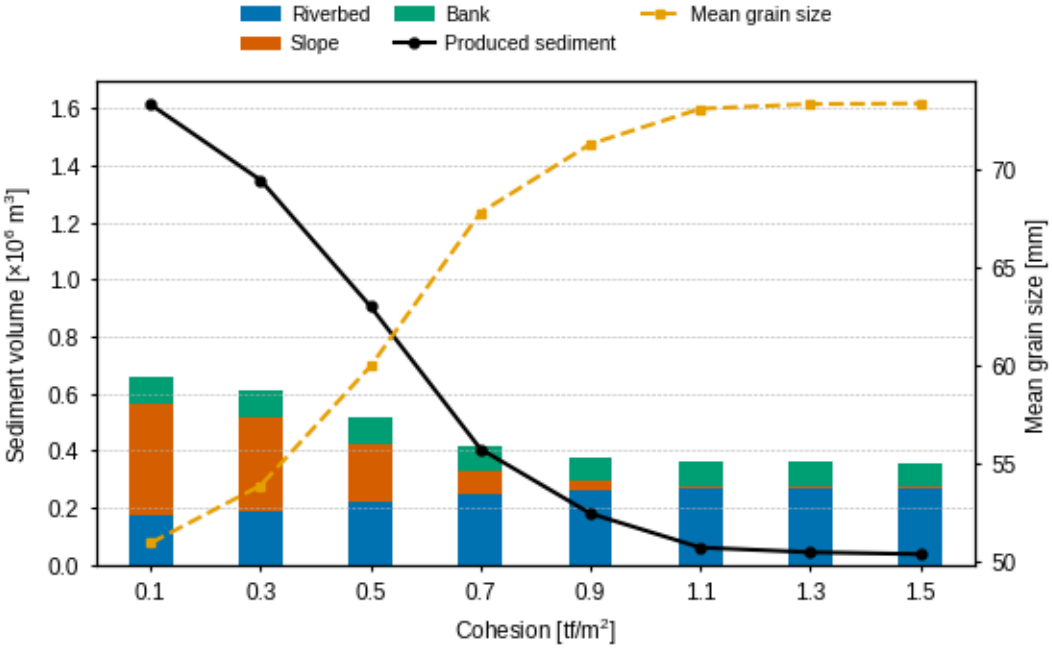

Figure 5: Results of SiMHiS simulations using cohesion and the estimated failure probability and saturation degree derived from machine learning models (RSF and RF). Stacked bar charts show sediment discharge from the downstream point by source, with blue indicating sediment from riverbed, orange indicating sediment from slope, and green indicating sediment from bank. The black line represents produced sediment by slope failure, and the orange line represents the average grain size of the discharged sediment.

https://doi.org/10.5194/egusphere-2026-2689
Preprint. Discussion started: 9 July 2026

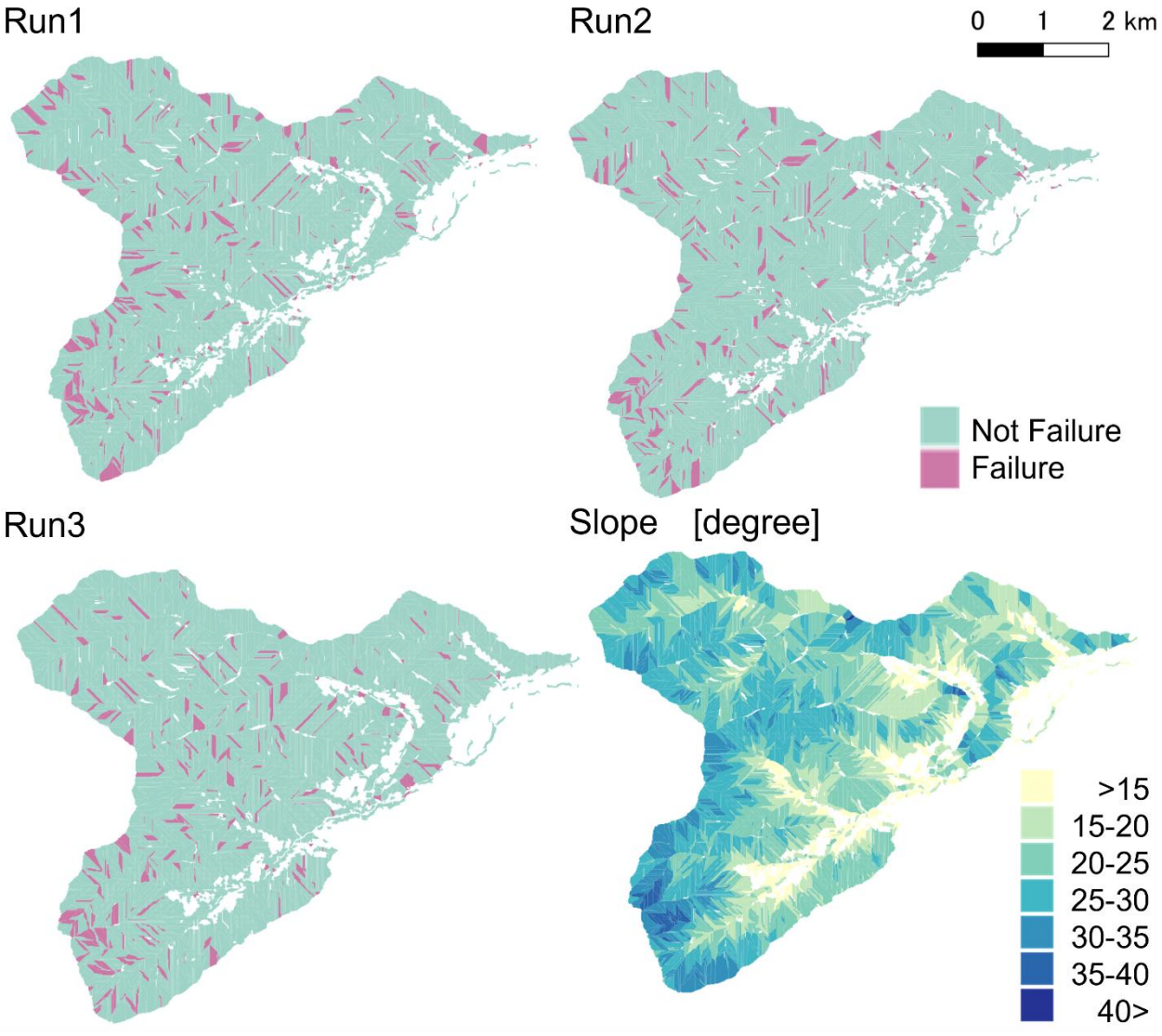

Figure 6: Spatial distribution of failed slopes for three simulations (Run 1–Run 3) conducted under identical conditions with a cohesion value of 0.95 tf/m² and slope gradient distribution. Green indicates stable slopes, and pink indicates failed slopes.

https://doi.org/10.5194/egusphere-2026-2689
Preprint. Discussion started: 9 July 2026

Table 2: Number of failed slope elements, produced sediment, and sediment discharge for three simulations (Run 1–Run 3) conducted under identical conditions (cohesion = 0.95 tf/m²)

	Number of failed slope elements	Produced sediment [m^3]	Sediment discharge [m^3]
Run1	315 (8.5%)	148,831	376,328
Run2	289 (7.8%)	151,608	375,262
Run3	281 (7.6%)	161,937	372,880

4 Discussion

In this study, we proposed a method that enables watershed-scale evaluation of slope failure occurrence and sediment production by training machine learning models on the results of rainfall infiltration–induced slope stability analyses. Sediment supplied from slope failures strongly influences sediment transport processes in river channels. In general, sediment derived from slopes is finer than bed material. The incorporation of fine sediment into the bed reduces the critical shear stress required for sediment transport (Egiazaroff 1965; Hirano 1971). Furthermore, when sediment supply exceeds the equilibrium transport capacity, deposition of fine particles alters the bed structure and frictional properties, potentially increasing transport capacity (John et al. 1999). Therefore, it is important to evaluate sediment production and transport at the watershed scale.

Several approaches have been proposed to evaluate rainfall-induced slope failure and sediment production at the watershed scale. The TRIGRS model (Baum et al. 2008) computes factor of safety at each grid cell based on pore-water pressure obtained from a one-dimensional Richards equation, allowing identification of unstable areas across a watershed. While computationally efficient, TRIGRS cannot estimate slip surfaces or landslide volume. Burton et al. (1998) developed a model that estimates critical saturation and landslide volume using fine-resolution stability calculations and empirically derived relationships and then couples these results with coarser-scale hydrological and sediment transport simulations. However, this model is difficult to apply to watersheds with different geotechnical conditions and assumes a unique critical saturation threshold without accounting for uncertainty. In contrast, the proposed method performs rainfall infiltration–slope stability analyses for a large number of slopes with varying topographic and geotechnical conditions, enabling probabilistic estimation of failure saturation and landslide volume. This approach allows efficient evaluation of sediment production processes at the watershed scale with relatively low computational cost, making it a promising tool for large-scale sediment disaster risk assessment. As shown in Figure 5, even under same rainfall conditions, the sediment discharge in the case with cohesion of 0.1 tf/m² is nearly 1.5 times larger than that in the case with 1.5 tf/m². This indicates that increased supply of fine sediment enhances the total sediment discharge from the watershed. In addition, changes in produced sediment alter the dominant sediment sources, which in turn

https://doi.org/10.5194/egusphere-2026-2689
Preprint. Discussion started: 9 July 2026

affects the average grain size of the discharged sediment. These results demonstrate that the proposed method enables estimation of both sediment supply and grain size, which are essential for watershed-scale sediment dynamics assessment.

Regarding slope failure prediction, this study estimated failure probability by using saturation ratio with four slope parameters (cohesion, internal friction angle, slope gradient, and slope length). Instead of providing a deterministic prediction, the model introduces probabilistic variability even under identical conditions. In general, more unstable slopes tend to fail at lower saturation ratio (Regmi, et al. 2010; Sujit et al. 2015). However, it is difficult to determine failure occurrence based on a single parameter alone (Çellek 2020), and interactions among multiple factors must be considered. In real slopes, additional factors such as vegetation, soil properties, land use, curvature, and elevation also affect stability (Budimir 2015). Although it is difficult to explicitly incorporate all these factors at the watershed scale, the proposed method indirectly accounts for such uncertainties by representing failure occurrence as a probability conditioned on saturation ratio. As a result, even slopes that are classified as stable based on input parameters retain a non-zero probability of failure, allowing rare failure events to be reproduced. This probabilistic representation is particularly effective for long-term simulations such as climate change prediction, where slope failures tend to initiate in highly unstable slopes and propagate progressively with inherent variability, rather than occurring uniformly across the landscape.

Regarding cohesion, laboratory tests yielded values in the range of 0.07–0.53 tf/m², whereas a value of 0.95 tf/m² provided the best agreement with observed sediment production. This discrepancy is likely due to additional cohesion provided by additional cohesion due to roots. Although the dominant tree species in the Pekerebetsu basin are unknown, the basin is widely forested. Additional cohesion due to roots depends on root diameter and density (Schmidt et al. 2001), and it in forested areas is typically reported in the range of 0.2–0.9 tf/m² (Schmidt et al. 2001; Wu et al. 1979; Hubble et al. 2013). Therefore, the value of 0.95 tf/m² can be considered reasonable when accounting for both soil and root cohesion. However, additional cohesion due to roots varies with vegetation type and exhibits depth-dependent distributions (Bischetti et al. 2009), and thus also depends on the location of the slip surface. Further investigation is required to incorporate spatial variability of root reinforcement and slip surface depth into the model.

For landslide volume estimation, this study predicted failure length from slope parameters and multiplied it by soil depth and slope width. As shown in Figure 2(c), failure length tends to converge to approximately 15–20 m when slope length exceeds 15 m. In particular, failure lengths exceeding 20 m were observed under relatively stable slope conditions. This is likely because failure occurs at higher saturation ratio, resulting in soil masses with higher water content and larger mobilized volumes. Similarly, Mukhlisin et al. (2008) reported that slopes with higher effective porosity are less prone to failure but tend to generate larger-scale landslides when failure occurs due to higher water content. These findings suggest that increased rainfall intensity under climate change may lead to unprecedented increases in landslide volume due to higher water content at failure.

In the Pekerebetsu basin simulation, soil depth was assumed to be spatially uniform. This assumption is supported by the strong empirical relationship between landslide volume V_L and landslide area A_L, commonly expressed as $V_L = \alpha A_L^{\beta}$ (Amirahmadi et al. 2016; Guzzetti et al. 2009; Rice and Foggin 1971; Imaizumi et al. 2008). Assuming a constant soil

https://doi.org/10.5194/egusphere-2026-2689
Preprint. Discussion started: 9 July 2026

depth D_s, landslide volume can be approximated as $V_L = A_L D_s$, implying a linear relationship between volume and area. Although the coefficients α and β vary among regions, they can often be approximated as constant within a single watershed, suggesting that the effect of spatial variability in soil depth is effectively incorporated into these empirical parameters. Therefore, assuming a uniform soil depth provides a reasonable approximation for watershed-scale sediment production estimation. However, there are limitations in the representation of slope width. In this study, slope width was defined as the slope area divided by slope length based on ridge–valley segmentation, whereas actual failure width depends strongly on failure mechanisms and terrain conditions. For example, Li et al. (2022) showed that failure width tends to decrease downslope due to lateral confinement. Future work should incorporate three-dimensional analyses that account for spatial variability in soil depth and lateral variations in failure width.

5 Conclusion

In this study, rainfall infiltration–slope stability analyses were conducted for slopes with diverse geotechnical and topographic conditions, and a machine learning model was developed using slope parameters together with the saturation ratio at failure and failure length as training data. The model enables the estimation of both the critical saturation at failure and the corresponding failure length directly from slope parameters.

The trained machine learning model was then applied to each slope elements within a watershed to estimate failure saturation and failure length, and these estimates were incorporated into a sediment production and transport model. This integration allows for the simulation of sediment production due to slope failures and subsequent sediment discharge at the watershed scale.

To estimate failure saturation, a probabilistic approach was adopted by predicting failure probability as a function of saturation. This framework enables the incorporation of uncertainties arising from factors not explicitly represented in the input parameters, such as spatial variability in soil depth and vegetation effects.

The proposed model was integrated into the sediment production and transport framework and applied to the Pekerebetsu River basin, successfully reproducing sediment production and discharge during the 2016 heavy rainfall event in Hokkaido.

https://doi.org/10.5194/egusphere-2026-2689
Preprint. Discussion started: 9 July 2026

Code and data availability

The data required to reproduce the figures and tables presented in this paper, together with the machine-learning scripts developed in this study, are available from Zenodo at https://doi.org/10.5281/zenodo.20118904. The repository includes the calculation results used for the figures, the training data generated from the rainfall infiltration–slope stability analyses, the machine-learning model outputs, and the scripts used to train and apply the machine-learning models.

Author contributions

RK, TI and KY designed the simulation, and RK carried them out. RK developed the model code and performed the simulations. RK prepared the manuscript with contributions from TI and KY.

Competing interests

The authors declare that they have no conflict of interest.

Financial support

We acknowledge support from JSPS KAKENHI Grant 23K22872, 24K21633 and 25KJ1865.

https://doi.org/10.5194/egusphere-2026-2689
Preprint. Discussion started: 9 July 2026

References

Aoki, D., Kasai, M., and Igura, M.: The Effects of Hydraulic Structures on Streams Prone to Bank Erosion in an Intense Flood Event: A Case Study from Eastern Hokkaido, in: Symposium Proceedings of the INTERPRAEVENT 2018 in the Pacific Rim, 270–275, 2018.

Amirahmadi, A., Pourhashemi, S., Karami, M., and Akbari, E.: Modeling of landslide volume estimation, Open Geosci., 8, 360–370, https://doi.org/10.1515/geo-2016-0032, 2016.

Ashida, K. and Michiue, M.: Study on hydraulic resistance and bed-load transport rate in alluvial streams, Proc. JSCE, 206, 59–69, 1972.

Baum, R. L., Savage, W. Z., and Godt, J. W.: TRIGRS—A Fortran program for transient rainfall infiltration and grid-based regional slope-stability analysis, version 2.0, U.S. Geological Survey Open-File Report, 2008–1159, 75 pp., 2008.

Biasutti, M., Seager, R., and Kirschbaum, D. B.: Landslides in West Coast metropolitan areas: the role of extreme weather events, Weather Clim. Extremes, 14, 67–79, https://doi.org/10.1016/j.wace.2016.11.004, 2016.

Bischetti, G. B., Chiaradia, E. A., Epis, T., and Morlotti, E.: Root cohesion of forest species in the Italian Alps, Plant Soil, 324, 71–89, https://doi.org/10.1007/s11104-009-9941-0, 2009.

Budimir, M. E. A., Atkinson, P. M., and Lewis, H. G.: A systematic review of landslide probability mapping using logistic regression, Landslides, 12, 419–436, https://doi.org/10.1007/s10346-014-0550-5, 2015.

Buffington, J. M. and Montgomery, D. R.: Effects of sediment supply on surface textures of gravel-bed rivers, Water Resour. Res., 35, 3523–3530, https://doi.org/10.1029/1999WR900232, 1999.

Bui, D. T., Moayedi, H., Gör, M., Jaafari, A., and Foong, L. K.: Predicting slope stability failure through machine learning paradigms, ISPRS Int. J. Geo-Inf., 8, 395, https://doi.org/10.3390/ijgi8090395, 2019.

Burton, A. and Bathurst, J. C.: Physically based modelling of shallow landslide sediment yield at a catchment scale, Environ. Geol., 35, 89–99, https://doi.org/10.1007/s002540050296, 1998.

Çellek, S.: Effect of the slope angle and its classification on landslide, Nat. Hazards Earth Syst. Sci. Discuss., 1–23, https://doi.org/10.5194/nhess-2020-87, 2020.

Chabokpour, J.: Enhancing bed load prediction accuracy through advanced multi-parameter analysis: a new temperature-sensitive approach validated across 783 river measurements, Stoch. Environ. Res. Risk Assess., 39, 3703–3721, https://doi.org/10.1007/s00477-025-03034-9, 2025.

Chen, C.-Y. and Fujita, M.: A method for predicting landslides on a basin scale using water content indicator, J. JSCE, Ser. B1 (Hydraul. Eng.), 70, I_13–I_18, https://doi.org/10.2208/jscejhe.70.I_13, 2014.

Egiazaroff, I. V.: Calculation of nonuniform sediment concentrations, J. Hydraul. Div., 91, 225–247, https://doi.org/10.1061/JYCEAJ.0001277, 1965.

https://doi.org/10.5194/egusphere-2026-2689
Preprint. Discussion started: 9 July 2026

Furuichi, T., Osanai, N., Hayashi, S.-i., Izumi, N., Kyuka, T., Shiono, Y., Miyazaki, T., Hayakawa, T., Nagano, N., and Matsuoka, N.: Disastrous sediment discharge due to typhoon-induced heavy rainfall over fossil periglacial catchments in western Tokachi, Hokkaido, northern Japan, Landslides, 15, 1645–1655, https://doi.org/10.1007/s10346-018-1005-1, 2018.

Godt, J. W., Baum, R. L., Savage, W. Z., Salciarini, D., Schulz, W. H., and Harp, E. L.: Transient deterministic shallow landslide modeling: requirements for susceptibility and hazard assessments in a GIS framework, Eng. Geol., 102, 214–226, https://doi.org/10.1016/j.enggeo.2008.03.019, 2008.

Guzzetti, F., Ardizzone, F., Cardinali, M., Rossi, M., and Valigi, D.: Landslide volumes and landslide mobilization rates in Umbria, central Italy, Earth Planet. Sci. Lett., 279, 222–229, https://doi.org/10.1016/j.epsl.2009.01.005, 2009.

Hirano, M.: River-bed degradation with armouring, Proc. JSCE, 195, 55–65, https://doi.org/10.2208/jscej1969.1971.195_55, 1971.

Hubble, T. C. T., Airey, D. W., Sealey, H. K., De Carli, E. V., and Clarke, S. L.: A little cohesion goes a long way: Estimating appropriate values of additional root cohesion for evaluating slope stability in the Eastern Australian highlands, Ecol. Eng., 61, 621–632, https://doi.org/10.1016/j.ecoleng.2013.07.069, 2013.

Imaizumi, F., Sidle, R. C., and Kamei, R.: Effects of forest harvesting on the occurrence of landslides and debris flows in steep terrain of central Japan, Earth Surf. Process. Landf., 33, 827–840, https://doi.org/10.1002/esp.1574, 2008.

Inoue, T., Mishra, J., and Parker, G.: Numerical simulations of meanders migrating laterally as they incise into bedrock, J. Geophys. Res. Earth Surf., 126, e2020JF005645, https://doi.org/10.1029/2020JF005645, 2021.

Itakura, T. and Kishi, T.: Open channel flow with suspended sediments, J. Hydraul. Div., 106, 1325–1343, https://doi.org/10.1061/JYCEAJ.0005483, 1980.

Iverson, R. M.: Landslide triggering by rain infiltration, Water Resour. Res., 36, 1897–1910, https://doi.org/10.1029/2000WR900090, 2000.

Johnson, J. P. L.: Gravel threshold of motion: a state function of sediment transport disequilibrium?, Earth Surf. Dynam., 4, 685–703, https://doi.org/10.5194/esurf-4-685-2016, 2016.

Kaplan, E. L. and Meier, P.: Nonparametric estimation from incomplete observations, J. Am. Stat. Assoc., 53, 457–481, https://doi.org/10.1080/01621459.1958.10501452, 1958.

Kido, R., Inoue, T., Hatono, M., and Yamanoi, K.: Assessing the impact of climate change on sediment discharge using a large ensemble rainfall dataset in Pekerebetsu River basin, Hokkaido, Prog. Earth Planet. Sci., 10, 36, https://doi.org/10.1186/s40645-023-00580-0, 2023.

Kido, R., Inoue, T., and Yamanoi, K.: Sediment transport model for mountainous area considering river width expansion due to bank erosion and hiding effect, Japanese Journal of JSCE, 81, 24-16056, https://doi.org/10.2208/jscejj.24-16056, 2025. (in Japanese and English abstract).

Kosugi, K.: Lognormal distribution model for unsaturated soil hydraulic properties, Water Resour. Res., 32, 2697–2703, https://doi.org/10.1029/96WR01776, 1996.

https://doi.org/10.5194/egusphere-2026-2689
Preprint. Discussion started: 9 July 2026

Li, L., Lan, H., Strom, A., and Macciotta, R.: Landslide longitudinal shape: a new concept for complementing landslide aspect ratio, Landslides, 19, 1143–1163, https://doi.org/10.1007/s10346-021-01828-w, 2022.

Mahmoodzadeh, A., Mohammadi, M., Farid Hama Ali, H., Ibrahim, H. H., Abdulhamid, S. N., and Nejati, H. R.: Prediction of safety factors for slope stability: comparison of machine learning techniques, Nat. Hazards, 111, 1771–1799, https://doi.org/10.1007/s11069-021-05115-8, 2022.

Mandal, S.: Assessing cohesion, friction angle and slope instability in the Shivkhola watershed of Darjiling Himalaya, Int. Res. J. Earth Sci., 3, 1–10, 2015.

McKay, M. D., Beckman, R. J., and Conover, W. J.: A comparison of three methods for selecting values of input variables in the analysis of output from a computer code, Technometrics, 42, 55–61, https://doi.org/10.1080/00401706.2000.10485979, 2000.

Meyer-Peter, E. and Müller, R.: Formulas for bed-load transport, in: Proceedings of the 2nd Congress of the International Association for Hydraulic Structures Research, Stockholm, 7–9 June 1948, 39–64, 1948.

Miyazaki, T., Sawada, M., Matsuoka, N., Tachikawa, Y., Takashima, S., Yoshida, Y., Hayashi, S.-i., Furuichi, T., Kasai, M., and Osanai, N.: Large sediment discharge caused by periglacial slope failures and erosion induced by Typhoon Lionrock (2016) in Pekerebetsu Creek, Hokkaido, Japan, Journal of the Japan Society of Erosion Control Engineering, 71, 22–33, https://doi.org/10.11475/sabo.71.2_22, 2018.

Moayedi, H., Bui, D. T., Kalantar, B., and Foong, L. K.: Machine-learning-based classification approaches toward recognizing slope stability failure, Appl. Sci., 9, 4638, https://doi.org/10.3390/app9214638, 2019.

Mukhlisin, M., Taha, M. R., and Kosugi, K.: Numerical analysis of effective soil porosity and soil thickness effects on slope stability at a hillslope of weathered granitic soil formation, Geosci. J., 12, 401–410, https://doi.org/10.1007/s12303-008-0039-0, 2008.

Posner, A. J. and Georgakakos, K. P.: Soil moisture and precipitation thresholds for real-time landslide prediction in El Salvador, Landslides, 12, 1179–1196, https://doi.org/10.1007/s10346-015-0618-x, 2015.

Regmi, N. R., Giardino, J. R., and Vitek, J. D.: Assessing susceptibility to landslides: using models to understand observed changes in slopes, Geomorphology, 122, 25–38, https://doi.org/10.1016/j.geomorph.2010.05.009, 2010.

Rice, R. M. and Foggin, G. T., III: Effects of high intensity storms on soil slippage on mountainous watersheds in southern California, Water Resour. Res., 7, 1485–1496, 1971.

River Bureau, Ministry of Land, Infrastructure, Transport and Tourism: Basic policy for river improvement of Tokachi River System River, Japan, 2006 (in Japanese).

Rubey, W. W.: Settling velocities of gravel, sand, and silt particles, Am. J. Sci., 25, 325–338, https://doi.org/10.2475/ajs.s5-25.148.325, 1933.

Sato, A., Hayashi, T., Hayashi, H., and Yamaki, M.: On the geotechnical properties of decomposed granite soil in Hokkaido, in: Proceedings of the 57th Hokkaido Branch Technical Report Meeting of the Japanese Geotechnical Society, No. 75, 2016 (in Japanese).

https://doi.org/10.5194/egusphere-2026-2689
Preprint. Discussion started: 9 July 2026

Schmidt, K. M., Roering, J. J., Stock, J. D., Dietrich, W. E., Montgomery, D. R., and Schaub, T.: The variability of root cohesion as an influence on shallow landslide susceptibility in the Oregon Coast Range, Can. Geotech. J., 38, 995–1024, https://doi.org/10.1139/cgj-38-5-995, 2001.

Shinohara, K. and Tsubaki, T.: On the characteristics of sand waves formed upon the beds of the open channels and rivers, Rep. Res. Inst. Appl. Mech., 7, 15–45, 1959.

Sofia, G. and Nikolopoulos, E. I.: Floods and rivers: a circular causality perspective, Sci. Rep., 10, 5175, https://doi.org/10.1038/s41598-020-61533-x, 2020.

Tsai, T.-L.: The influence of rainstorm pattern on shallow landslide, Environ. Geol., 53, 1563–1569, https://doi.org/10.1007/s00254-007-0767-x, 2008.

Tsutsumi, D. and Fujita, M.: Relative importance of slope material properties and timing of rainfall for the occurrence of landslides, Int. J. Erosion Control Eng., 1, 79–89, 2008.

Wicki, A., Lehmann, P., Hauck, C., Seneviratne, S. I., Waldner, P., and Stähli, M.: Assessing the potential of soil moisture measurements for regional landslide early warning, Landslides, 17, 1881–1896, https://doi.org/10.1007/s10346-020-01400-y, 2020.

Wu, T. H., McKinnell, W. P., III, and Swanston, D. N.: Strength of tree roots and landslides on Prince of Wales Island, Alaska, Can. Geotech. J., 16, 19–33, https://doi.org/10.1139/t79-003, 1979.

Xie, M., Esaki, T., Zhou, G., and Mitani, Y.: Geographic Information Systems-Based Three-Dimensional Critical Slope Stability Analysis and Landslide Hazard Assessment, J. Geotech. Geoenviron. Eng., 129, 1109–1118, https://doi.org/10.1061/(ASCE)1090-0241(2003)129:12(1109), 2003.

Xu, H., He, X., and Sheng, D.: Rainfall-induced landslides from initialization to post-failure flows: stochastic analysis with machine learning, Mathematics, 10, 4426, https://doi.org/10.3390/math10234426, 2022.

Yamanoi, K. and Fujita, M.: Development of a combined model of sediment production, supply and transport, and its application to a mountainous basin, J. JSCE, 3, 224–229, https://doi.org/10.2208/journalofjsce.3.1_224, 2015.

Yamanoi, K. and Fujita, M.: Risk estimation of multiple hazards related to sediment and water disasters occurring in heavy rainfall, Journal of Japan Society of Civil Engineers, Ser. B1 (Hydraulic Engineering), 72, I_1291–I_1296, https://doi.org/10.2208/jscejhe.72.I_1291, 2016a.

Yamanoi, K. and Fujita, M.: Study on warning and evacuation system during sediment disaster in mountainous area employing multi-hazard simulator, Journal of the Japan Society of Erosion Control Engineering, 69, 15–23, https://doi.org/10.11475/sabo.69.6_15, 2016b.